

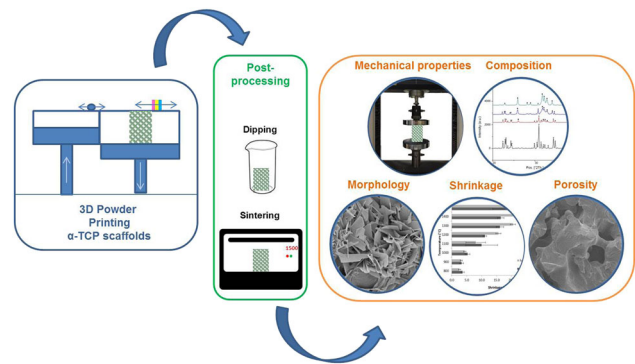
Different post-processing conditions for 3D bioprinted α -tricalcium phosphate scaffolds

Liciane Sabadin Bertol¹ · Rodrigo Schabbach¹ · Luis Alberto Loureiro dos Santos¹

Received: 25 April 2017 / Accepted: 5 September 2017 / Published online: 15 September 2017
© Springer Science+Business Media, LLC 2017

Abstract The development of 3D printing hardware, software and materials has enabled the production of bone substitute scaffolds for tissue engineering. Calcium phosphates cements, such as those based on α -tricalcium phosphate (α -TCP), have recognized properties of osteoinductivity, osteoconductivity and resorbability and can be used to 3D print scaffolds to support and induce tissue formation and be replaced by natural bone. At present, however, the mechanical properties found for 3D printed bone scaffolds are only satisfactory for non-load bearing applications. This study varied the post-processing conditions of the 3D powder printing process of α -TCP cement scaffolds by either immersing the parts into binder, Ringer's solution or phosphoric acid, or by sintering in temperatures ranging from 800 to 1500 °C. The porosity, composition (phase changes), morphology, shrinkage and compressive strength were evaluated. The mechanical strength of the post-processed 3D printed scaffolds increased compared to the green parts and was in the range of the trabecular bone. Although the mechanical properties achieved are still low, the high porosity presented by the scaffolds can potentially result in greater bone ingrowth. The phases present in the scaffolds after the post-processing treatments were calcium-deficient hydroxyapatite, brushite, monetite, and unreacted α -TCP. Due to their chemical composition, the 3D printed scaffolds are expected to be resorbable, osteoinductive, and osteoconductive.

Graphical abstract



1 Introduction

In most cases when craniofacial bone reconstruction is needed, the restoration of function and aesthetic contour are the main goals. There are different techniques and several materials currently available for this purpose, such as autologous bone flaps, allograft bone, xenograft bone, titanium, polymethylmethacrylate (PMMA), bioceramics such as hydroxyapatite (HA), polyethylene, biodegradable polymers [1, 2]. Each material has advantages and disadvantages, and the search for an ideal material continues.

Major bone reconstruction procedures often use autogenous grafts to improve bone healing; these bone grafts, however, suffer from multiple limitations (e.g. limited by the availability of suitable donor site especially for large defects, additional expensive surgery, tissue harvesting problems, donor site morbidity, chances of infection at the

✉ Liciane Sabadin Bertol
liciane.bertol@ufrgs.br

¹ Laboratory of Biomaterials (Labiomat), Materials Department, Federal University of Rio Grande do Sul, Av. Bento Gonçalves, 9500, 91501-970 Porto Alegre, RS, Brazil

recipient and donor sites, increased surgical time, resorption of the graft) that make synthetic alternatives an attractive option.

Some synthetic biocompatible bone substitutes have been developed to promote bone regeneration as alternatives to autogenous bone grafts [3]. Driven by the demand for efficient and full repair of bone defects, bioactive ceramics and its composites are advancing toward to high mechanical strength, good bioactivity and controlled biodegradation [4]. Calcium phosphates are a primary focus for synthetic bone graft substitutes because they are osteoconductive and provide sufficient mechanical strength [5]. In contrast to metals and polymers, several calcium phosphates spontaneously bind to living bone, and therefore their use as a 3D structure to support bone tissue formation (scaffold) is self-evident [6].

Even though these materials often present good clinical results, they have often fail to mimic the 3D anatomy and biology of native tissues. This limitation has subsequently led to the development of Additive Manufacture (AM) technologies. The enhancements of AM processes and software for 3D image analysis have enabled the direct production of anatomical models from computed tomography scans, which also permit the 3D visualization of the patient's bone structure and therefore enable surgical planning and the development of scaffolds designed for patient-specific geometries. These technologies are quickly becoming the techniques of choice for bone tissue regeneration procedures and scaffold fabrication, with the potential for overcoming the limitations of conventional fabrication techniques. AM technologies have also been at the forefront of the design and fabrication of porous materials, which allows the production of porous scaffolds with complex geometries containing internal pore architecture [4, 7–9] and a contour that fits to the patient's anatomy [10–15], addressing most of the requirements for tissue engineering (TE) applications. The challenge in scaffold-based TE is to construct biological replicas in vitro such that the engineered composite becomes integrated for transplantation in vivo for the recovery of loss or malfunctioned tissues or organ. The composite should subsequently function coordinately with the rest of the body without risk of rejection or complications [16].

Among the AM techniques, 3D powder printing (3DP) receives emphasis, in which three-dimensional objects are created through repetitive deposition and processing of material layers using computer-controlled equipment. It is based on the 2D cross-sectional data obtained from slicing a computer-aided design model of the object [17]. In 3D powder printing, a solid is generated by the reaction of a liquid selectively sprayed onto a powder bed. This liquid can either act as a binder or provoke a reaction that will bind the powder particles together. Once hardened, the layer is

covered with a new powder layer and successive 2D profiles are then printed on a freshly laid layer of powder until the whole model is completed. The structure is supported throughout the process by the surrounded unprocessed powder, which means that the powder bed acts not only as reagent but also as a physical support for the printed solid.

After the printing, the parts must be removed from the printer, cleaned, and post-processed to improve their mechanical properties. The stability of the parts obtained from powder-binder reaction can be enhanced by either a post-printing hardening regime (such as immersing the samples in a binder) or by sintering, leading to thermal decomposition. Sintering has an impact on the composition, mechanical properties and structural properties (shrinkage) of the materials [6].

Synthetic bone substitutes, in particular calcium phosphate powder, which can be used to generate 3D printed bone scaffolds, are considered particularly interesting solutions for bone tissue repair [3]. In the 3D powder printing of calcium phosphate cements, the binder dissolves the powder particles and new crystals form and interdigitate to form a stiff ceramic network [6].

Among the calcium phosphate cements, α -TCP (α -tricalcium phosphate, $\text{Ca}_3(\text{PO}_4)_2$) cement has received attention from the biological point of view due to its in vivo and in vitro non-toxicity, osteoconductivity and bioactivity. Besides, it is biodegradable and bioresorbable. This makes α -TCP cement an ideal implant material, able to be replaced by new bone faster than the other calcium-phosphate-based materials available in the market [18]. Despite a large number of formulations, all calcium orthophosphates form only two different end products: CDHA (calcium deficient hydroxyapatite, $\text{Ca}_9(\text{PO}_4)_5(\text{HPO}_4)(\text{OH})$) and DCP (dicalcium phosphate, CaHPO_4 , dihydrate or anhydrous). α -TCP forms CDHA upon contact with an aqueous solution. Upon mixing with water, the initial calcium orthophosphates are dissolved and precipitated into less soluble calcium orthophosphates, which causes the cement to set. During the precipitation reaction, new crystals grow and become entangled, thus providing mechanical rigidity to the cement [19]. When α -TCP cement is mixed with acidic solutions (below around pH 4.2), the dihydrate (also known as brushite) and anhydrous (also known as monetite) forms of dicalcium phosphate are the most stable (insoluble) of the calcium phosphates.

Low temperature 3D printing of calcium phosphate scaffolds holds great promise for fabricating synthetic bone graft substitutes with enhanced performance over traditional techniques [5]. Due to its known favourable biological properties, the use of TCP cement for 3D printing of bone scaffolds has been of great interest to the scientific community [20–25]. Although the characteristics of the process permit the fabrication of α -TCP cement parts, many design

parameters, such as the binder solution properties, have yet to be optimized to ensure maximal biocompatibility and osteoconductivity with adequate mechanical properties [5, 22]. The post-processing conditions required for 3DP processed parts, such as dipping or sintering, are also an opportunity for improvements in the fabrication of porous scaffolds. For ceramics, the most critical issue that needs attention is the mechanical behaviour of porous scaffolds [22], since many studies point to the use of calcium phosphate printed parts only for non-load bearing applications [6, 22, 23, 25–29]. Extensive process-property optimization is still needed. In this sense, this study is focused on identifying the influence of different post-processing conditions, not reported in the literature, on the physical and mechanical properties of α -TCP 3DP scaffolds.

2 Materials and methods

In order to evaluate the influence of different post-processing conditions in the mechanical and physical properties of α -tricalcium phosphate cement parts produced by 3D printing, the process steps are shown in Fig. 1 and subsequently described.

2.1 Process steps

2.1.1 Powder and binder preparation

α -TCP was synthesized by heating dicalcium phosphate dihydrate (DCPD, $\text{CaHPO}_4 \cdot 2\text{H}_2\text{O}$) for 5 h at 550 °C in a muffle furnace to obtain γ -calcium pyrophosphate (γ -CPP, $\text{Ca}_2\text{P}_2\text{O}_7$). After that, the powder was sieved (passing through a standard 200 mesh), mixed with CaCO_3 for 20 min and sintered at 1500 °C for 3 h. After synthesis, the powder was crushed in a mortar and pestle and

subsequently sieved (passing through a standard 200 mesh). After this point, the powder is referred to as cement.

The binder used to 3D print the parts was an aqueous solution of 2.5 wt% disodium hydrogen phosphate (Na_2HPO_4), used to accelerate the setting reaction of the cement. During the setting, it is expected that the hydrolysis of α -TCP results in calcium-deficient hydroxyapatite (CDHA) according to the reaction shown in Eq. 1. This equation is characteristic of the apatite cements.

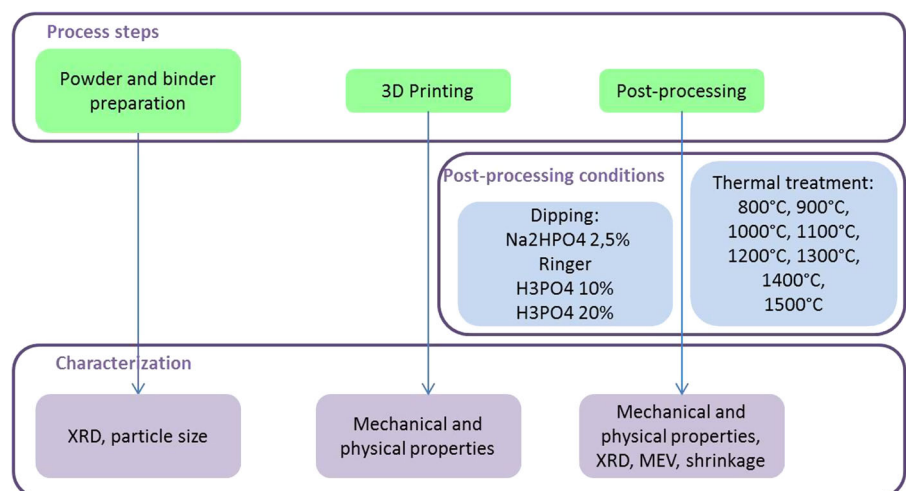


Approximately 2 kg of powder and 2 L of binder were prepared and used for the 3D printing of the specimens.

2.1.2 3D printing

The printing of cement samples was performed with a commercial 3D-powder printing system (Z-Printer 310 Plus, Z-Corporation, USA) using the α -TCP cement powder and an aqueous solution of 2.5 wt% Na_2HPO_4 as the binder. Although different definitions for the term “binder” exist, in this paper we refer to the Na_2HPO_4 solution as the “binder”. The 3D models (bulk cylinders of 24 mm height and 12 mm diameter) were imported in STL (stereolithography) format from CAD software. The printing parameters were chosen according to previous studies and maintained constant for all printing tests. The printing parameters were set to a layer thickness of 88 μm and a binder/volume ratio of 0.19 for the shell and 0.09 for the core of the 3DP part. The cylinders were printed along the y-axis, with the symmetry axis orthogonal to the powder bed surface. No adaptation of the commercial 3D printer was needed, since the binder solution used here did not affect the fluid lines and binder container. The printhead was C4800A (HP10 black print-head, ink drop size 35pl).

Fig. 1 Schematic overview of the process steps, evaluated post-processing conditions and characterization



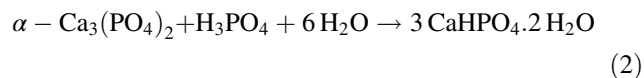
2.1.3 Post-processing

The 3D printed parts embedded in the loose powder must be extracted from the powder bed after they have been printed. For this, compressed air from the depowdering station was used to remove the unbound powder from their pores and cavities and clean the parts.

2.1.3.1 Dipping In order to complete the setting reaction and harden the 3D printed parts, after the depowdering they were immersed in different solutions for different time periods, as shown in Table 1.

One of the solutions was the aqueous solution of Na_2HPO_4 with a concentration of 2.5 wt%, the same as that used as the binder for the 3D printing. The Ringer's solution contains sodium chloride, potassium chloride, calcium chloride, and sodium bicarbonate in the concentrations in which they occur in body fluids. The other two studied post-processing solutions were phosphoric acid 10 and 20 wt%. It is important to notice that the parts immersed in phosphoric acid solution were previously immersed into the binder solution (Na_2HPO_4) for 14 days. Only after this period they were dipped into the phosphoric acid solution.

For the treatment by dipping the parts into H_3PO_4 solution, the expected reaction is expressed by Eq. 2, the typical reaction for brushite cements. Phosphoric acid partially dissolves the α -TCP powder particles, and these two compounds precipitate locally, resulting in the calcium phosphate phases of brushite (DCPD, $\text{CaHPO}_4 \cdot 2\text{H}_2\text{O}$) and monetite (DCPA, CaHPO_4), known for their excellent *in vivo* behavior [7].



2.1.3.2 Sintering After the immersion of the 3D printed scaffolds into the binder solution (Na_2HPO_4 2.5 wt%) for 14 days, an extra post-processing was executed aiming to enhance their mechanical properties. The samples were heated until the temperatures of 800 °C, 900 °C, 1000 °C, 1100 °C, 1200 °C, 1300 °C, 1400 °C, 1500 °C at a rate of 10 °C/min and maintained at the target temperature for 1 h.

Table 1 Solutions and immersion times used to post-process the 3D printed cylinders

Solution	Na_2HPO_4 2.5 wt%	Ringer	H_3PO_4 10 wt%	H_3PO_4 20 wt%
Immersion time	14 days	7 days	30 s (2×)	30 s (2×)

2.2 Material and structural characterization

2.2.1 Particle size distribution

The particle size distribution of the initial powder was measured with an 1180 Cilas Analyser using isopropyl alcohol as the liquid phase.

2.2.2 X-Ray diffraction

The crystalline composition of the initial powder (used for the 3D printing), the printed green parts, as well as the post-processed printed objects, was determined by XRD. A Phillips XPert diffractometer MPD with $\text{CuK}\alpha$ radiation (1.5418 Å) and voltage and current adjusted to 40 kV and 40 mA, respectively, was used to obtain the X-ray diffraction patterns and identify the crystalline compounds. Data were collected from $2\theta = 20^\circ$ – 40° with a step size of 0.02° and a normalized count time of 2 s/step.

2.2.3 Mechanical and physical testing

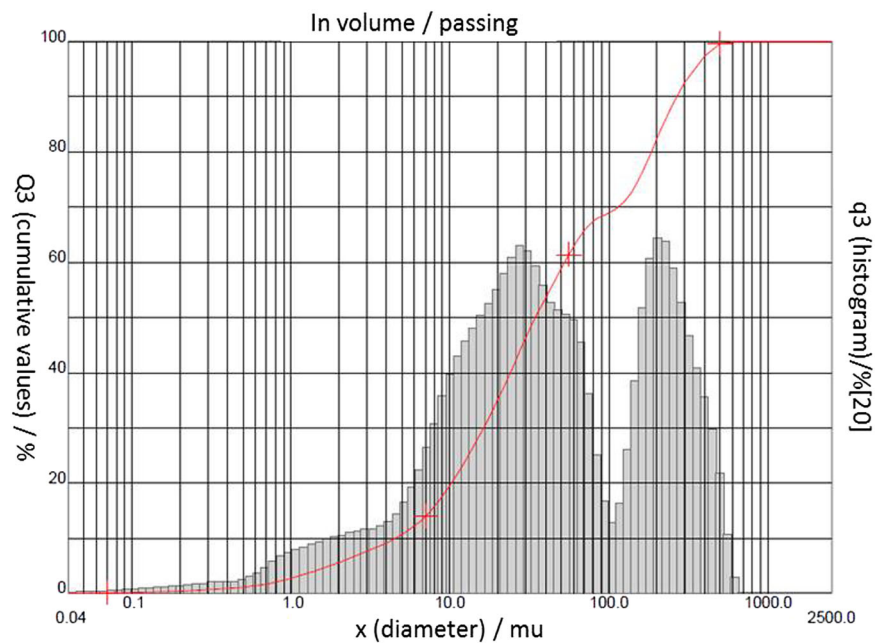
The compression strength of the 3D printed scaffolds was determined right after the 3DP and after post-processing. Ten cylinders were tested for every group, using an axial testing system (Instron Model 3369) with a 2 KN load cell. For the determination of the compression strength and the effective Young's modulus (elastic constant), the cylinders were tested at a cross-head speed of 1 mm/min.

Both before and after the post-processing, the apparent porosity and density of the printed cylinders were determined using Archimedes' principle, weighing them before and after filling the pores with water. In order to determine the average shrinkage of the printed scaffolds submitted to temperatures from 800 °C to 1500 °C, measurements were made of their height and diameter at three different locations using a micrometer, before and after sintering.

2.2.4 Scanning electron microscopy

Scanning electron microscopy (SEM, equipment JEOL model JSM6060) was used to access the morphology of the parts obtained after the different post-processing conditions. The samples were previously sputtered with a thin layer of carbon.

Fig. 2 Histogram plot of powder particle size distribution



3 Results

3.1 Material and Structural Characterization

3.1.1 Particle size distribution

A medium particle diameter of 92.45 μm , was found for the initial obtained α -TCP cement powder. The histogram plot of powder particle size distribution is shown in Fig. 2. The particle size distribution was found to be suitable for 3D printing, with good powder bed smoothness.

3.1.2 X-Ray diffraction

The comparative results of the X-ray diffraction patterns of the powders present at different stages of the process are shown in Fig. 3: the initial powder (used to print the parts), the green parts (right after 3D printing) and post-processed printed parts (after dipping the samples in Na_2HPO_4 2.5 wt% and Ringer's solution). It is possible to observe different degrees of reaction for the analysed powders.

For the initial powder (synthesized using γ -calcium pyrophosphate and CaCO_3 as precursors) used to 3D print the cylinders, the phase composition was checked by means of the JCPDS reference patterns for α -TCP (PDF Ref. 09-0348 and 029-0359). There were no peaks corresponding to other calcium phosphate phases.

As can be seen in Fig. 3, the powder obtained after the 3D printing (referred to as the 3D printed powder) presents a diffraction pattern very similar to the initial powder, showing many peaks corresponding to the initial α -TCP powder. The diffraction pattern corresponding to the 3D

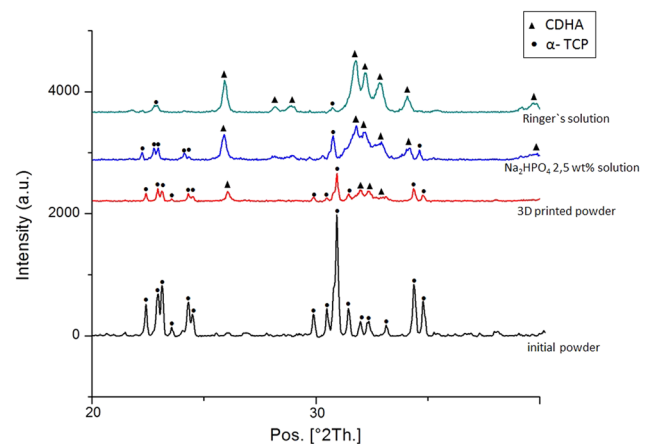


Fig. 3 Comparison of XRD patterns of the initial powder and 3D printed parts—just after printing and after dipping in Na_2HPO_4 2.5 wt% and Ringer's solutions

printed powder refers to calcium deficient hydroxyapatite (PDF Ref. 010896438) and unreacted α -TCP (PDF Ref. 09-0348 and 029-0359).

The immersion of the parts into a binder solution (Na_2HPO_4 2.5 wt%) increased the degree of reaction and formation of hydroxyapatite. However, the quantity of unreacted α -TCP powder still remains high when compared with the immersion of the printed parts in Ringer's solution. The higher degree of transformation of α -TCP into CDHA after the immersion in either aqueous solution (binder and Ringer's solution) can be noticed. However, low-intensity peaks corresponding to the precursor cement powder still appear, indicating an incomplete transformation after the time of immersion.

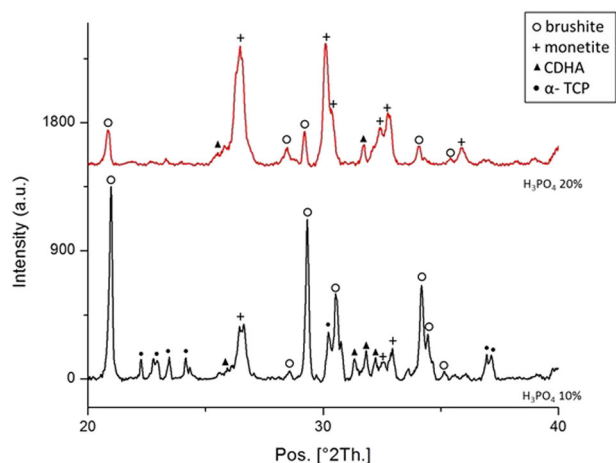


Fig. 4 Comparison of XRD patterns of the 3D printed parts after dipping in H_3PO_4 10 wt% and 20 wt%

The crystalline phases formed in the 3D printed parts immersed in phosphoric acid solutions are shown in Fig. 4. The setting of the printed parts has occurred via an acid base reaction between the α -TCP powder and the phosphoric acid, which leads to the formation of brushite and monetite according to Eq. 2. The crystalline phases of brushite and monetite correspond to the standard files JCPDS 009.0077 and 009.0080 respectively. Although they appear as peaks of low intensity, an amount of unreacted α -TCP can still be found, as well as hydroxyapatite, formed during the 3D printing process.

3.1.3 Mechanical testing

Ten cylinders of each group (printed green parts, as well as the post-processed parts—dipped in Na_2HPO_4 , Ringer and H_3PO_4 solutions—were compressed until failure. The results for the mechanical testing of the solid cylinders are expressed in terms of compressive strength and are summarized in Fig. 5.

For the apatitic cements, the maximum average compressive strength was presented by the printed parts dipped in Ringer's solution, and reached 1.14 MPa. The scaffolds post-treated with phosphoric acid presented higher values for compressive strength, reaching 2.70 ± 0.32 MPa and 5.01 ± 1.02 MPa for the dipping solutions H_3PO_4 wt. 20 and 10%, respectively. The post-processing treatment of immersion of the printed parts in phosphoric acid increased the reaction of TCP into brushite and monetite and decreased the porosity and the α -TCP content. This explains the higher compressive strength of these post-processed scaffolds compared to the values for the printed green samples.

After the sintering, the printed parts were also submitted to compressive strength measurements. The scaffolds were

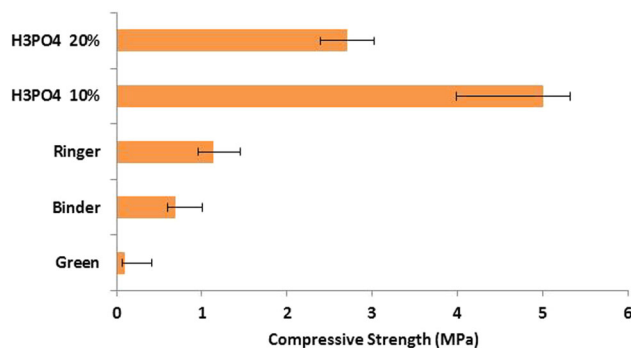


Fig. 5 Comparison of average compressive strengths of the 3D printed parts, before and after post-processing by immersion

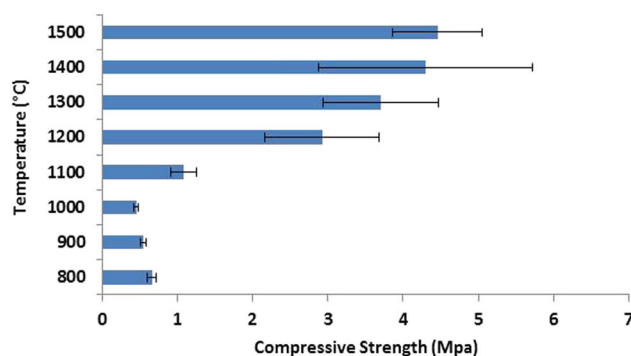


Fig. 6 Comparison of the average compressive strength of the 3D printed parts, before and after post-processing by sintering

submitted to temperatures ranging from 800 to 1500 °C and 5 parts submitted to each temperature were tested. The average results are summarized in Fig. 6.

The thermal treatment to which the parts were subjected caused a gradual thermal decomposition of the CDHA phase and the formation of pyrophosphate, in temperatures up to around 1100 °C. Above this temperature, the most stable phase becomes β -tricalcium phosphate ($Ca_3(PO_4)_2$, JCPDS 009.0169), which can be retained during cooling to room temperature. Based on this, it is possible to explain the decrease in mechanical strength of the parts subjected to heat treatment up to a certain temperature. Above this temperature, an increase in mechanical strength can be noticed. The ultimate tensile strength obtained for the sintered scaffolds increased gradually with the increase of temperature and achieved a maximum value of 4.46 ± 0.6 MPa at 1500 °C, evidencing its densification at higher temperatures.

3.1.4 Porosity

Table 2 shows the calculated porosities and apparent densities for the cement 3D scaffolds post-treated with the studied solutions, and after sintering.

Table 2 Apparent density and total porosity of printed scaffolds after different post-processing conditions

Sample condition	Apparent density (g/cm ³)	Apparent porosity (%)
Green	0.82 (±0.02)	69.8 (±0.6)
Immersion	Na ₂ HPO ₄ 2.5 wt% 14 days	0.87 (±0.12) 58.4 (±6.0)
	Ringer's solution 7 days	0.83 (±0.01) 64.3 (±0.4)
	H ₃ PO ₄ 10 wt% 2 × 30 s	1.05 (±0.01) 52.5 (±0.3)
	H ₃ PO ₄ 20 wt% 2 × 30 s	1.13 (±0.02) 52.0 (±1.1)
Sintering	800 °C 1 h	0.94 (±0.03) 63.5 (±1.2)
	900 °C 1 h	0.97 (±0.02) 63.1 (±0.4)
	1000 °C 1 h	0.95 (±0.02) 65.1 (±0.9)
	1100 °C 1 h	1.16 (±0.01) 58.7 (±0.3)
	1200 °C 1 h	1.40 (±0.02) 51.1 (±0.7)
	1300 °C 1 h	1.62 (±0.04) 43.9 (±1.1)
	1400 °C 1 h	1.75 (±0.04) 38.7 (±1.4)
	1500 °C 1 h	1.89 (±0.13) 31.4 (±3.1)

The immersion of the scaffolds in different solutions resulted in a reduction of the porosity and an increase of the apparent density, since the degree of reaction of α-TCP into the reaction products has risen. For the thermally treated scaffolds, there was an increase in density and reduction in porosity with an increase of sintering temperature, which led to the increase in mechanical properties by the reduction of the spaces between the powder particles.

3.1.5 Shrinkage

Due to the large voids between the particles in the green state, significant sintering shrinkage can occur, as illustrated in Fig. 7. Measurements of scaffolds prior to and post-sintering revealed that the shrinkage in the longitudinal direction was greater than the reduction in the radial direction for parts post-treated up to 1200 °C. The average shrinkage values presented by the printed scaffolds were lower than 10% (both in diameter and height) when submitted to temperatures up to 1000 °C. At greater temperatures, this value increases gradually, reaching the maximum value of 28% for longitudinal retraction at 1500 °C. With a temperature increase, the spaces between the powder particles decrease, consequently reducing the part's porosity and increasing its density.

Since shrinkage is highly reproducible, the final shrinkage must be compensated for by scaling the 3D CAD model prior to transferring the virtual model to the 3D printer.

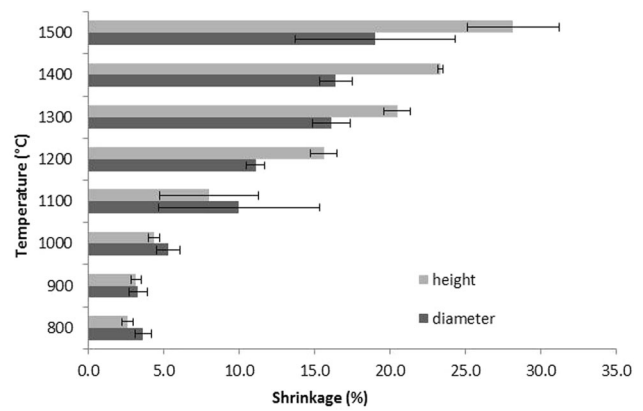


Fig. 7 Average shrinkage presented by the printed scaffolds submitted to temperatures ranging from 800 to 1500 °C

3.1.6 Scanning electron microscopy

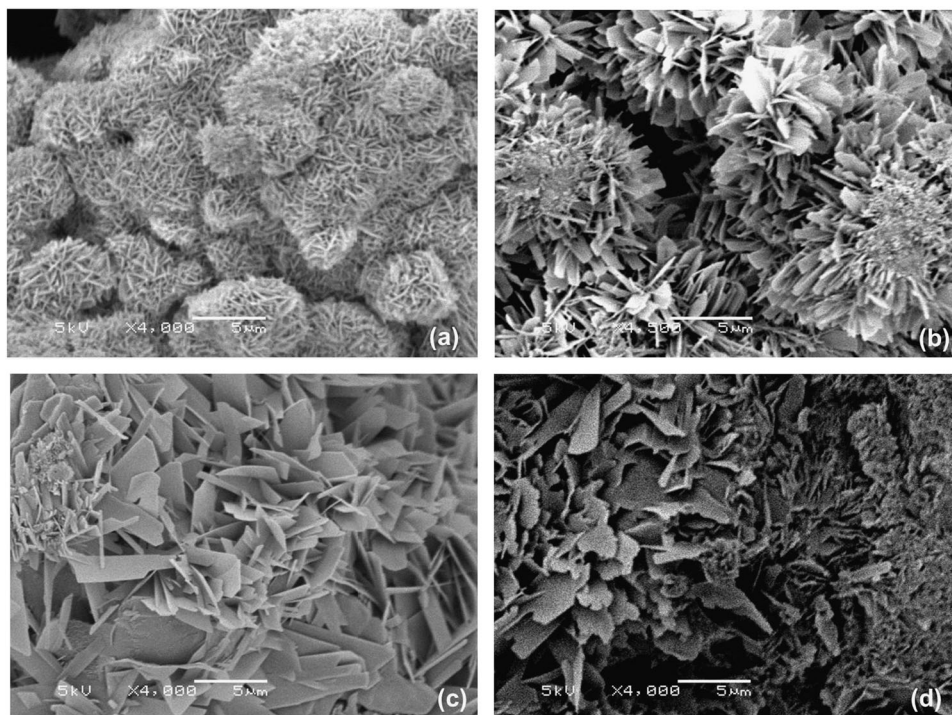
Different results are found when hydrolysis of α-TCP is performed using an aqueous solution, or when the transformation of α-TCP is being performed using H₃PO₄, which has been proved by the XRD analysis. To address this point, the 3D printed scaffolds, after being immersed in different solutions, were analysed by SEM in order to evaluate the morphology of the obtained structures, as depicted in Fig. 8.

During the setting mechanisms of the cements, initiated in the 3D printing process and continued in the post-processing by immersion of the parts, the powder is dissolved by the binder solution and the particles are bound via subsequent recrystallization. Different crystal structures can be noticed for apatite and brushite cements, those generated by reaction with aqueous solutions (binder and Ringer) and acidic solutions (phosphoric acid).

The α-TCP parts post-processed with binder (Na₂HPO₄ 2.5 wt%) and Ringer's solution presented a petal or needle-like morphology. Through their setting, CDHA precipitates and forms an entanglement of CDHA crystals. The interlocking of these structures explains the increase in mechanical strength presented by hydroxyapatite, in comparison to the green parts. In (a), there is a morphology with spherical clusters formed by smaller needles. The size of the crystals and their entanglement as well, are smaller than in (b), which explains the difference in the mechanical properties. Interparticle pores can also be noticed.

The post-treatment, consisting of immersing the printed parts in phosphoric acid, on the other hand, results in flatter and larger crystals, formed by the dissolution of the precursors and precipitation of brushite and monetite. Precipitated brushite crystals often develop large crystals, enhancing mechanical entanglement, resulting in cements with greater strength than those with smaller and less entangled monetite crystals [7]. For the samples immersed in H₃PO₄ 20% solution (d), a smaller amount reacted into

Fig. 8 SEM micrographs of α -TCP printed parts after setting by immersion in **a** Na_2HPO_4 2.5 wt%, **b** Ringer, **c** H_3PO_4 10 wt% and **d** H_3PO_4 20 wt%



the brushite phase, explaining the lower mechanical strength of the parts in comparison with those immersed in H_3PO_4 10% solution (c).

For the sintered samples, it is possible to notice in the SEM images a significant decrease in pore size and porosity, shown in Fig. 9. An enlargement of crystal size is also remarkable, and becomes evident above 1200 °C. Up to this temperature, the initial unbounded powder particles from the 3D printing process are still apparent.

4 Discussion

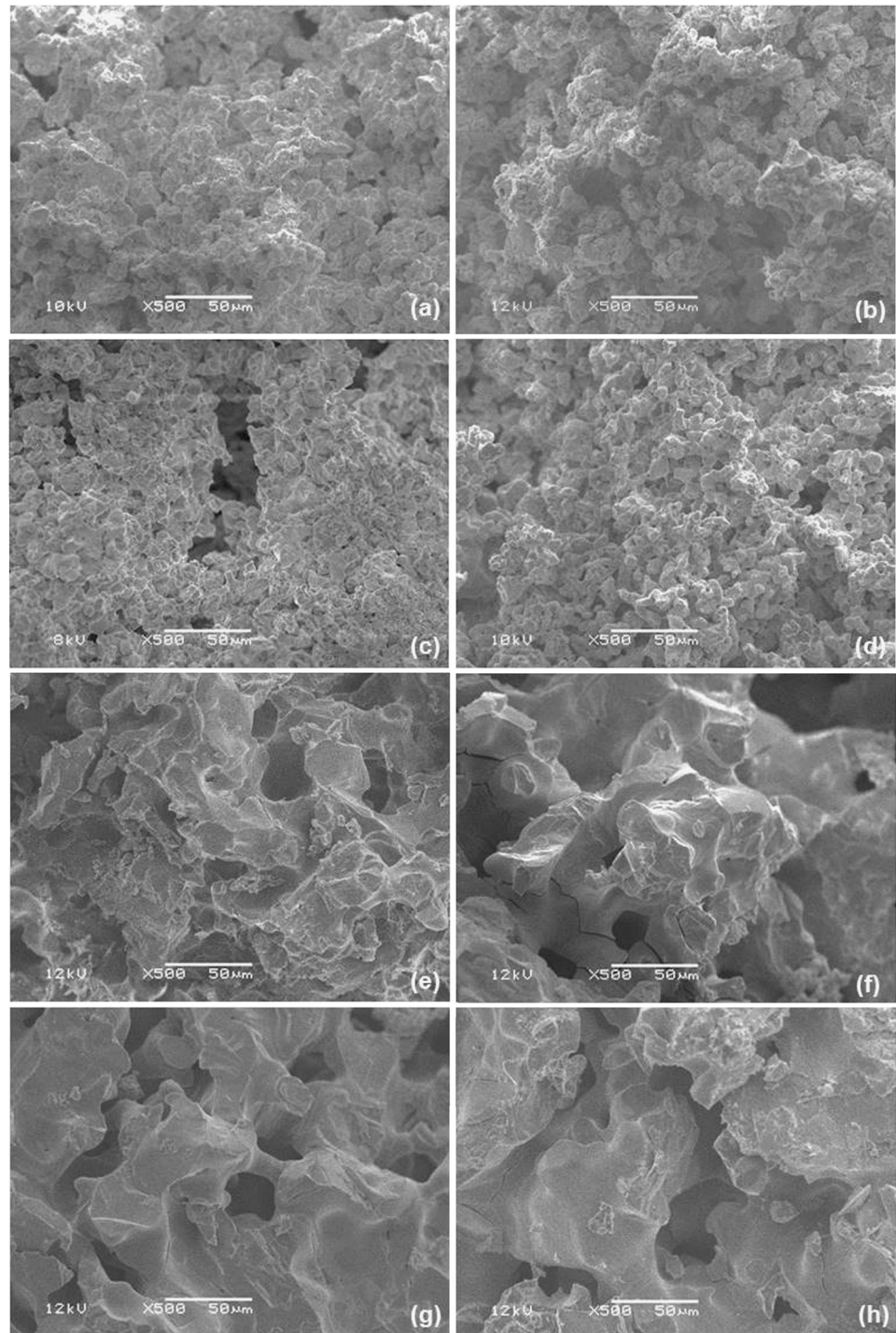
The XRD results revealed that only a small portion of the α -TCP powder reacted into calcium deficient hydroxyapatite in the 3D printing process itself. CDHA is a biocompatible and osteoconductive calcium-phosphate material, and is characterized by a high similarity to natural human bone in its chemical composition and morphology. It may be defined as a biomimetic framework because it is recognised as “self” by the recipient bone, thus avoiding any immunological reaction [30]. After the 3D printing, a great quantity of unreacted powder remains present in the sample. This might be explained by the fact that the quantity of liquid that is dropped into the powder bed is not enough to wet the powder particles. Considering this, the reaction of hydrolysis of the calcium phosphate and formation of CDHA was not completed for the whole amount of the powder. Additionally, it has been reported that the reactivity

of α -TCP decreases with the reduction of the surface area of the powder [31]. In this way, the high particle size used in this study might have reduced the kinetics of formation of CDHA.

The immersion of the 3D printed α -TCP scaffolds in binder and Ringer’s solution increased the degree of reaction (Fig. 3). The setting reaction of an apatitic cement mixed with a Na_2HPO_4 2.5 wt% liquid phase had been evaluated and the complete disappearance of α -TCP peaks after 15 days immersion in Ringer’s solution had been reported previously [32]. Although hydroxyapatite has limited in vivo resorption and remodeling capacity [28], these materials are expected to be osteoconductive, osteoinductive and resorbable in vivo due to their chemical composition of hydroxyapatite and unreacted tricalcium phosphate.

As can be observed in the XRD (Fig. 4), there is a difference in the proportion between the crystalline phases found for scaffolds immersed in phosphoric acid solution 10 or 20 wt%. The formation of a greater or lesser amount of brushite or monetite may vary according to the pH of the solution. However, although the most stable calcium phosphate at pH from about 4.2 is monetite, brushite is preferably formed due to its reaction kinetics, which is higher than that of monetite [33]. The preferential formation of brushite occurred for samples immersed in H_3PO_4 10 wt% solution. The higher concentration of the phosphoric solution increased the degree of reaction, where peaks of the precursor α -TCP powder can no

Fig. 9 SEM micrographs of thermally post-processed scaffolds in different temperatures for 1 h. **a** 800 °C, **b** 900 °C, **c** 1000 °C, **d** 1100 °C, **e** 1200 °C, **f** 1300 °C, **g** 1400 °C, **h** 1500 °C



longer be found. The formation of monetite is however, favoured.

It has been demonstrated that the acidic calcium phosphates (brushite and monetite) are osteoconductive, osteoinductive and resorb faster than hydroxyapatite, which is of great interest for maxillofacial bone augmentation [34]. Nevertheless, *in vivo*, brushite tends to reprecipitate as insoluble hydroxyapatite, slowing its replacement by bone.

Monetite is slightly less soluble and appears not to transform to hydroxyapatite [28]. These biomaterials appear to be promising for several bone regeneration strategies due to their favourable properties in a physiological environment, besides being able to be 3D printed with specific internal and external structures.

Green strength refers to the initial strength after printing. As previously described [35], the binder adsorption and the

mechanical interlocking are the two binding mechanisms that dictate the mechanical properties of the green part. This is a very important property of the printed scaffold and will affect the final strength. It describes the mechanical characteristics immediately after extraction from the powder bed and subsequent depowdering. Insufficient green strength may result in shape changes or mechanical failure of the green part [6]. The removal of the parts and subsequent depowdering were critical since the printed green parts were very easy to break when manipulated. For these weak scaffold structures, even the weight of the unbound powder was critical. This lack of stability, in addition to the mechanical testing of the 3DP printed green parts, revealed the necessity for post-hardening steps after 3DP, since the average compressive strength of the scaffolds before post-processing was 0.11 MPa. Nevertheless, the mechanical stability of the green parts still must be improved.

The different post-processing treatments increased significantly the compressive strength of the printed scaffolds, when compared to the green ones. The mechanical properties achieved by the post-processed parts were in the range of the trabecular bone, that can range from around 2 to 38 MPa [27]. However, the low mechanical strength is still a major challenge for the α -TCP scaffolds and limits their use to only non-load bearing applications.

A wide range of values of the compressive strength of 3D printed scaffolds have already been reported in the literature. The compressive green strength of porous HA green scaffolds has been reported to be 0.88 ± 0.02 MPa [36]. Butscher et al. [7] has found ultimate compressive strength from 1.9 to 8.4 MPa for α -TCP printed bulk cylinders, varying the post-processing methods, and between 0.26 and 1.24 MPa for porous scaffolds. Gbureck et al. [21] have reported compressive strengths of dicalcium phosphates between 0.9 and 8.7 MPa depending on the acid concentration, and reaching 22 MPa after extra post-hardening. This evidences the constant need for research and optimization in the process and materials, since related studies still point to the use of the 3D printed TCP scaffolds as not suitable for cases when structural support is required.

Although the post processing using H_3PO_4 succeeded better in terms of an increase of mechanical strength, removing the toxic elements at the end of the printing process continues to be a problem [3]. The residual acidity may be removed by thoroughly rinsing the scaffolds. Besides, when used directly as binder during the 3D printing process [25, 28, 37], the phosphoric acid significantly compromises the printhead performance and requires adaptations in the 3D printer such as changing the binder fluid lines [5, 7]. In this study, however, no adaptation in the 3D printer was needed, since an aqueous neutral solution was used as binder.

Undoubtedly, there is a need for porosity to permit the functionalization of the scaffold so that it fulfills its requirements for bone regeneration. The morphology of the natural bone is composed of cortical bone, with a porous environment with 3–12% porosity, and trabecular bone, with 50–90% porosity. In vitro, the scaffold's lower porosities stimulate osteogenesis by suppressing cell proliferation and forcing cell aggregation. On the other hand, higher porosity results in greater bone ingrowth [38]. This trend, however, results in diminished mechanical properties, thereby setting limit values for the porosity.

It has been shown in the literature that the pore size and porosity have a great influence on the compressive strength, with reported values of compressive strength around 3.0 MPa for α/β -TCP 3DP scaffolds conventionally sintered at 1250 °C with 1000 μ m pore size. With a decrease in pore size and porosity, higher values were achieved, reaching 6.4 MPa for 500 μ m pore size [39].

Mechanical strength is required to meet the demands on the properties of scaffolds. The printed parts, even post-processed, presented high porosity but low mechanical strength and therefore low mechanical integrity. Generally, higher values for apparent density result in better mechanical properties. However, the rapid vascularization of scaffolds is favoured by more porous and therefore weaker structures [40]. A high porosity of around 40–60% is desired [6]. The high porosity could be potentially beneficial for cell attachment due to the increased surface area [41]. It may also increase surface accessibility for the fluid, thus accelerating the dissolution of the scaffold [42].

5 Conclusions

In this study, different post-processing conditions for scaffolds produced by 3D printing in α -TCP were evaluated. The 3D parts were produced in a commercial 3D printer using Na_2HPO_4 2.5 wt% as binder, and no adaptations in the printer were necessary. The immersion of the printed green parts in the binder and Ringer's solution increased the degree of transformation of α -TCP into calcium deficient hydroxyapatite. However, some quantity of unreacted α -TCP still remained in the post-processed scaffolds. These post-processing treatments increased the mechanical strength and decreased the porosity, when compared to the green parts.

The post-processing treatment, consisting in immersion of the 3D printed green parts in phosphoric acid, decreased the porosity and the α -TCP content and increased the reaction of TCP into brushite and monetite. It was possible to obtain higher compressive strength and lower porosity of the post-hardened scaffolds with respect to the values of

printed green parts and immersion in the binder and Ringer's solution.

The thermal treatment of the 3D printed scaffolds increased their compressive strength in comparison to the green parts and reduced significantly their porosity. The shrinkage achieved a maximum value of 28% for thermal treatment at 1500 °C. Due to its reproducibility, it can be compensated for by scaling the 3D virtual model before printing.

In general, the mechanical properties of the post-processed 3D printed scaffolds were in the range of the trabecular bone. Although the mechanical properties presented are limited, the higher porosity results in greater bone ingrowth. The scaffolds are sufficiently strong for handling and placement into a non-loading bone defect. Due to their chemical composition, they are expected to be resorbable, osteoconductive and osteoconductive, which allows the replacement and incorporation of these scaffolds into the newly forming bone.

Acknowledgements The authors would like to thank the National Institute of Biofabrication (INCT-BIOFABRIS), Brazil. This work was supported by CNPq (Conselho Nacional de Desenvolvimento Científico e Tecnológico, Brazil) and FINEP (Financiadora de Estudos e Projetos, Brazil).

Compliance with ethical standards

Conflict of interest The authors declare that they have no competing interests.

References

1. Gerbino G, Biachi FA, Zavattoni E, Tartara F, Garbossa D, Ducati A. Single-step resection and reconstruction using patient-specific implants in the treatment of benign cranio-orbital tumors. *J Oral Maxillofac Surg*. 2013; <https://doi.org/10.1016/j.joms.2013.03.021>.
2. Parthasarathy J. 3D modeling, custom implants and its future perspectives in craniofacial surgery. *Annals Maxillofac Surg*. 2014; <https://doi.org/10.4103/2231-0746.133065>.
3. Brunello G, Sivoletta S, Meneghello R, Ferroni L, Gardin C, Piattelli A, Zavan B, Bressan E. Powder-based 3D printing for bone tissue engineering. *Biotechnol Adv*. 2016; <https://doi.org/10.1016/j.biotechadv.2016.03.009>.
4. Shao H, He Y, Fu J, He D, Yang X, Xie J, Yao C, Ye J, Xu S, Gou Z. 3D printing magnesium-doped wollastonite/B-TCP bioceramics scaffolds with high strength and adjustable degradation. *J Eur Ceram Soc*. 2016; <https://doi.org/10.1016/j.jeurceramsoc.2016.01.010>.
5. Inzana JA, Olvera D, Fuller SM, Kelly JP, Graeve OA, Schwartz EM, Kates SL, Awad HA. 3D Printing of composite calcium phosphate and collagen scaffolds for bone regeneration. *Biomaterials*. 2014; <https://doi.org/10.1016/j.biomaterials.2014.01.064>.
6. Butscher A, Bohner M, Hofmann S, Gaucler L, Müller R. Structural and material approaches to bone tissue engineering in powder-based three-dimensional printing. *Acta Biomater*. 2011; <https://doi.org/10.1016/j.actbio.2010.09.039>.
7. Butscher A, Bohner M, Doebelin N, Hofmann S, Müller R. New depowdering-friendly designs for three-dimensional printing of calcium phosphate bone substitutes. *Acta Biomater*. 2013; <https://doi.org/10.1016/j.actbio.2013.07.019>.
8. Montazerian H, Davoodi E, Asadi-Eydivand M, Kadkhodapour J, Solati-Hashjin M. Porous scaffold internal architecture design based on minimal surfaces: a compromise between permeability and elastic properties. *Mater Des*. 2017; <https://doi.org/10.1016/j.matdes.2017.04.009>.
9. Afshar M, Anaraki AP, Montazerian H, Kadkhodapour J. Additive manufacturing and mechanical characterization of graded porosity scaffolds designed based on triply periodic minimal surface architectures. *J Mech Behav Biomed Mater*. 2016; <https://doi.org/10.1016/j.jmbbm.2016.05.027>.
10. Munsch M. Laser additive manufacturing of customized prosthetics and implants for biomedical applications. In: Brandt M, editor. *Laser Additive Manufacturing - Materials, Design, Technologies, and Applications*, Woodhead Publishing Series in Electronic and Optical Materials. Cambridge, UK: Elsevier Science & Technology, 2017. p. 399–420.
11. Jardim LA, Larosa MA, Kaasi A, Kharmandayan P. Additive manufacturing in medicine. *Ref Module Mater Sci Mater Eng*. 2017; <https://doi.org/10.1016/B978-0-12-803581-8.04152-7>.
12. Jardini AL, Larosa MA, Maciel Filho R, Zavaglia AAC, Bernardes LF, Lambert CS, Calderoni DR, Kharmandayana P. Cranial reconstruction: 3D biomodel and custom-built implant created using additive manufacturing. *J Cranio-Maxillofac Surg*. 2014; <https://doi.org/10.1016/j.jcms.2014.07.006>.
13. Rachmiel A, Shilo D, Blanc O, Emodi O. Reconstruction of complex mandibular defects using integrated dental custom-made titanium implants. *Br J Oral Maxillofac Surg*. 2017; <https://doi.org/10.1016/j.bjoms.2017.01.006>.
14. Bertol LS, Kindlein Jr W, Silva FP, Aumund-Kopp K. Medical design: direct metal laser sintering of Ti-6Al-4V. *Mater Des*. 2010; <https://doi.org/10.1016/j.matdes.2010.02.050>.
15. Visscher DO, Farre-Guasch E, Helder MN, Gibbs S, Forouzanfar T, van Zuijlen PP, Wolff J. Advances in bioprinting technologies for craniofacial reconstruction. *Trends Biotechnol*. 2016; <https://doi.org/10.1016/j.tibtech.2016.04.001>.
16. Leong KF, Cheah CM, Chua CK. Solid freeform fabrication of three-dimensional scaffolds for engineering replacement of tissues and organs. *Biomaterials*. 2003; [https://doi.org/10.1016/S0142-9612\(03\)00030-9](https://doi.org/10.1016/S0142-9612(03)00030-9).
17. Lam CXF, Mo XM, Teoh SH, Hutmacher DW. Scaffold development using 3D printing with a starch-based polymer. *Mater Sci Eng C*. 2002; [https://doi.org/10.1016/S0928-4931\(02\)00012-7](https://doi.org/10.1016/S0928-4931(02)00012-7).
18. Carrodegua RG, De Aza S. α -Tricalcium phosphate: synthesis, properties and biomedical applications. *Acta Biomater*. 2011; <https://doi.org/10.1016/j.actbio.2011.06.019>.
19. Dorozhkin SV. Bioceramics of calcium orthophosphates. *Biomaterials*. 2010; <https://doi.org/10.1016/j.biomaterials.2009.11.050>.
20. Castilho M, Dias M, Vorndran E, Gbureck U, Fernandes P, Pires I, Gouveia B, Armés H, Pires E, Rodrigues J. Application of a 3D printed customized implant for canine cruciate ligament treatment by tibial tuberosity advancement. *Biofabrication*. 2014; <https://doi.org/10.1088/1758-5082/6/2/025005>.
21. Gbureck U, Hozel T, Klammert U, Wurzler K, Muller FA, Baralet JE. Resorbable dicalcium phosphate bone substitutes prepared by 3D powder printing. *Adv Funct Mater*. 2007; <https://doi.org/10.1002/adfm.200700019>.
22. Bose S, Vahabzadeh S, Bandyopadhyay A. Bone tissue engineering using 3D printing. *Mater Today*. 2013; <https://doi.org/10.1016/j.mattod.2013.11.017>.
23. Almela T, Brook IM, Khoshroo K, Rasoulianboroujeni M, Fahimipour F, Tahriri M, Dashtimoghdam E, El-Awa A, Tayebi L,

- Moharamzadeh K. Simulation of cortico-cancellous bone structure by 3D printing of bilayer calcium phosphate-based scaffolds. *Bioprinting*. 2017; <https://doi.org/10.1016/j.bprint.2017.04.001>.
24. Bertol LS, Schabbach R, Santos LAL. Dimensional evaluation of patient-specific 3D printing using calcium phosphate cement for craniofacial bone reconstruction. *J Biomater Appl*. 2017; <https://doi.org/10.1177/0885328216682672>.
 25. Klammert U, Gbureck U, Vorndran E, Rödiger J, Meyer-Marcotty P, Kübler AC. 3D powder printed calcium phosphate implants for reconstruction of cranial and maxillofacial defects. *J Cranio-Maxillofac Surg*. 2010; <https://doi.org/10.1016/j.jcms.2010.01.009>.
 26. Burguera EF, Xu HH, Takagi S, Chow LC. High early strength calcium phosphate bone cement: effects of dicalcium phosphate dihydrate and absorbable fibers. *J Biomed Mater Res*. 2005; <https://doi.org/10.1002/jbm.a.30497>.
 27. Mauffrey C, Seligson D, Lichte P, Pape HC, Al-Rayyan M. Bone graft substitutes for articular support and metaphyseal comminution: what are the options? *Injury, Int J Care Injured*. 2011; <https://doi.org/10.1016/j.injury.2011.06.012>.
 28. Tamimi F, Torres J, Gbureck U, Lopez-Cabarcos E, Bassett DC, Alkhraisat MH, Barralet J. Craniofacial vertical bone augmentation: a comparison between 3D printed monolithic monetite blocks and autologous onlay grafts in the rabbit. *Biomaterials*. 2009; <https://doi.org/10.1016/j.biomaterials.2009.07.049>.
 29. Bergmann C, Lindner M, Zhang W, Koczurischer H. 3D printing of bone substitute implants using calcium phosphate and bioactive glasses. *J Eur Ceram Soc*. 2010; <https://doi.org/10.1016/j.jeurceramsoc.2010.04.037>.
 30. Staffa G, Barbanera A, Faiola A, Fricia M, Limoni P, Mottaran R, Zanotti B, Stefini R. Custom made bioceramic implants in complex and large cranial reconstruction: a two-year follow-up. *J Cranio-Maxillofac Surg*. 2012; <https://doi.org/10.1016/j.jcms.2011.04.014>.
 31. Durucan C, Brown PW. Reactivity of alpha-tricalcium phosphate. *J Mater Sci*. 2002; <https://doi.org/10.1023/A:1014347814241>.
 32. Ginebra MP, Fernandez E, De Maeyer EAP, Verbeeck RMH, Boltong MG, Ginebra J, Driessens FCM, Planell JA. Setting reaction and hardening of an apatitic calcium phosphate cement. *J Dent Res*. 1997; <https://doi.org/10.1177/00220345970760041201>.
 33. Cama G. Calcium phosphate cements for bone regeneration. In: Dubruel P, Van Vlierberghe S, editors. *Biomaterials for bone regeneration*. Cambridge, UK: Woodhead Publishing; 2014. p. 3–25.
 34. Tamimi F, Torres J, Lopez-Cabarcos E, Bassett DC, Habibovic P, Luceron E, Barralet JE. Minimally invasive maxillofacial vertical bone augmentation using brushite based cements. *Biomaterials*. 2009; <https://doi.org/10.1016/j.biomaterials.2008.09.032>.
 35. Uhland SA, Holman RK, Morissette S, Cima MJ, Sachs EM. Strength of green ceramics with low binder content. *J Am Ceram Soc*. 2001; <https://doi.org/10.1111/j.1151-2916.2001.tb01098.x>.
 36. Cox CS, Thornby JA, Gibbons GJ, Williams MA, Mallick KK. 3D printing of porous hydroxyapatite scaffolds intended for use in bone tissue applications. *Mater Sci Eng C*. <https://doi.org/10.1016/j.msec.2014.11.024>.
 37. Butscher A, Böhner M, Roth C, Ernstberger A, Heuberger R, Doebelin N, Rohr PR, Müller R. Printability of calcium phosphate powders for three-dimensional printing of tissue engineering scaffolds. *Acta Biomater*. 2012; <https://doi.org/10.1016/j.actbio.2011.08.027>.
 38. Karageorgiou V, Kaplan D. Porosity of 3D biomaterial scaffolds and osteogenesis. *Biomaterials*. 2005; <https://doi.org/10.1016/j.biomaterials.2005.02.002>.
 39. Tarafder S, Balla VK, Davies NM, Bandyopadhyay A, Bose S. Microwave-sintered 3D printed tricalcium phosphate scaffolds for bone tissue engineering. *J Tissue Eng Regen Med*. 2012; <https://doi.org/10.1002/term.555>.
 40. Will J, Melcher R, Treul C, Travitzky N, Kneser U, Polykandriotis E, Horch R, Greil P. Porous ceramic bone scaffolds for vascularized bone tissue regeneration. *J Mater Sci Mater Med*. 2008; <https://doi.org/10.1007/s10856-007-3346-5>.
 41. Zhou Z, Buchanan F, Mitchell C, Dunne N. Printability of calcium phosphate: calcium sulphate powders for the application of tissue engineered bone scaffolds using the 3D printing technique. *Mater Sci Eng C*. 2014; <https://doi.org/10.1016/j.msec.2014.01.027>.
 42. Leukers B, Gülkan H, Irsen SH, Milz S, Tille C, Schieker M, Seitz H. Hydroxyapatite scaffolds for bone tissue engineering made by 3D printing. *J Mater Sci Mater Med*. 2005; <https://doi.org/10.1007/s10856-005-4716-5>.